Measurement of bone quality using multispectral X-ray imaging with Medipix3 detectors

Andrea García-Tejedor Bilbao-Goyoaga
Utrecht University
Nikhef
Amsterdam, Netherlands
a.garcia-tejedor@students.uu.nl

***Abstract*—Osteoporosis is a common disease that affects bone strength and leads to an increased risk of fracture, resulting in lower quality of life. Bone Mineral Density (BMD) is a widespread parameter in the assessment and early diagnosis of osteoporosis. The current methods to quantify BMD and bone quality are limited since they do not take into account the complete composition of characteristic tissues that influence the bone's resistance to fracture. Medipix3 detectors, have high-resolution photon-counting technology and can acquire images at multiple energy thresholds simultaneously, which could be very useful in determining the different tissues of which bone is composed and their density. This project presents a pipeline for a first approach to material separation using Medipix3 detectors in known samples. It describes an energy threshold calibration method that improves the reconstruction of the thickness and overall shape of a sample and is then used to distinguish different materials and their proportion in a sample with three plastics, evaluating its usability and studying its limitations. Results show that this pipeline is capable of decomposing materials for simulated data, but more research is needed to success this task with real data since the contribution of many physical phenomena and their influence on image quality need to be studied and systematically accounted for. This setup has a lot of potential for being used in clinical practice for the assessment of osteoporosis.**

***Index Terms*—Bone Mineral Density, osteoporosis, Medipix3, X-Rays, spectroscopy, medical imaging**

1. INTRODUCTION

Osteoporosis is a prevalent bone disease that affects 6% of men and 21% of women within the age range of 50 to 84 in the European Union (EU) alone [1]. This condition is primarily characterized by the progressive weakening of bone structure, resulting in heightened fragility and an elevated risk of fractures, which can lead to excruciating pain, reduced quality of life, disability, and even mortality for those affected.

The accurate and early diagnosis of osteoporosis is essential for effective prevention and management of fragility fractures. The strength and integrity of bone tissue depend on its mineral content, particularly the presence of calcium and phosphate, which contribute to the formation and maintenance of a strong bone matrix. Disruption of the balance between bone formation and resorption can result in a low Bone Mineral Density (BMD), which is a widely used measurement related to risk of fractures, morbidity, mortality, and socioeconomic burden associated with osteoporosis [2]. The current gold standard for measuring BMD is Dual-energy X-ray absorptiometry (DXA), because of its reproducibility, non-invasive nature, and short acquisition time [3]. It functions by emitting X-rays at two distinct energies. These X-rays are absorbed differently by the different tissues. By measuring the differential attenuation of these X-rays, DXA can distinguish and quantify the density and composition of these tissues. This enables precise assessments of BMD and body composition. However, it has limitations such as radiation exposure, and limited accuracy in certain populations [4]. DXA has been documented to yield misleading measurements in several research studies [5], [6]. Quantitative Computed Tomography (QCT) is an alternative method, very valuable when DXA measurements may not be sufficient or feasible. Its main features are the increased accuracy and volumetric BMD measurement, providing information about the size and shape of the bone in addition to the areal density. However, the radiation exposure is much higher, its availability is limited and phantoms are often needed.

Thus, there is a need for new methods that can provide accurate and sensitive measurements of bone quality. New techniques have arisen in the last years to help overcome the limitations of DXA and QCT methods for BMD measurement [7]. High-resolution peripheral quantitative computed tomography (HR-pQCT) was introduced as a tool for assessing bone quality [8]. This imaging technique can provide detailed, three-dimensional imaging and quantitative measurements of bone microarchitecture and density at peripheral skeletal sites. It offers valuable insights into bone quality and fracture risk but still suffers from limitations in terms of radiation exposure, limited accessibility, and potential image artifacts [9].

Previous studies have demonstrated the potential of multispectral X-ray imaging in the bio-medical field [10] and in the task of basis material classification [11]. However, these studies have typically relied on conventional X-ray detectors that are limited in their ability to accurately measure the attenuation properties of bone tissue. Consequently, such studies have fallen short of providing in-depth insights into the microstructure and composition of bone tissue. Medipix3 detectors [12], on the other hand, have high-resolution photon-counting technology and can acquire images at multiple energy thresholds simultaneously, allowing for very accurate detection of X-rays and the characterization of materials based on their energy-dependent attenuation properties [13], [14]. Originally developed for particle physics experiments, they have since been adapted for a variety of applications. The present study seeks to assess the potential of Medipix3 detectors in an X-ray setup for the precise determination of bone compounds in healthy bone tissue. The primary objective is to achieve a more accurate measurement of bone quality by exploiting the unique capabilities of Medipix3 detectors. This study will limit its scope to plastic tissues to comprehensively evaluate the potentials and limitations of utilizing Medipix3 detectors in the task of identifying and quantifying the characteristic tissues of the bone that influence its resistance to fracture.

2. OBJECTIVES

The overall objective of this research is to analyze to which extent the Medipix3 detectors can contribute to identifying the different elements that bones are composed of for quantifying BMD. As the described application is new, the experiments will focus on measuring the set-up capability to determine the ratio of the presence of different compounds in a sample with 2D X-rays.

3. MATERIALS & METHODS

The experiments were carried out in Nikhef the Dutch National Institute for Subatomic Physics [15] within the Detectors Research & Development department. The experimental set-up and software resources were provided by Nikhef and the used samples were provided by Nikhef and University Medical Center of Utrecht [16]. In this section, a pipeline will be described in which a threshold calibration method for Medipix3 was first implemented and tested with an image of PEEK ($C_{19}H_{14}O_3$) plastic and then applied as a step in the task of material decomposition for a slab of three glued plastics. In the end, some bone samples were imaged as a first approach to a medical application of this pipeline.

3.1 Experimental Setup

The X-ray cabinet is a sealed fire-safe cage closed with interlocks and lead cladding. Figure 1 shows an image of the experimental setup for this project with the open cabinet. It consists of an X-ray tube located in the red box, a holder for the object, and the Medipix3 detector.

The X-rays are generated in a standard X-ray tube with a tungsten anode. When the accelerated high energy electrons in the cathode collide with the anode, they produce Bremsstrahlung radiation in addition to characteristic X-rays [17].

The objects to be imaged are placed between the X-ray tube and the detector. The object holder must not interfere with the beam and should not be placed in the Field of View. To keep the object isolated for imaging, it was wrapped in very thin foil and held in the sides as shown in Figure 1. During the course of this project, different phantoms were imaged. The details of the phantom materials are shown in Table I.

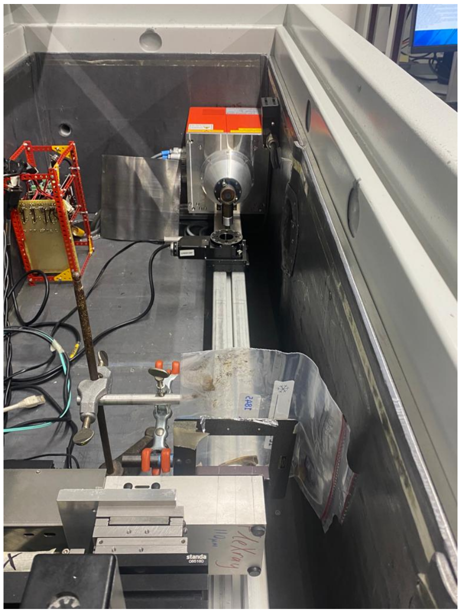

Fig. 1: *A picture of the open X-ray cabinet showing the experimental set-up for the image acquisition of a sample. The X-ray tube at the top, the detector at the bottom, and the object and the holder in the middle.*

Name	Chemical formula	Density(ρ)[gr/cm^3]
Polycarbonate	$C_{15}H_{16}O_2$	1.2
Plexiglas	$C_5O_2H_8$	1,18
Polyether ether ketone (PEEK)	$C_{19}H_{14}O_3$	1.31
Graphite	C	2.25
Vinyl polymer (PVC)	C_2H_3Cl	1.45
Teflon	C_2F_4	2.2

TABLE I: *Chemical formula and density of the imaged plastics.*

Medipix3 is a hybrid pixel detector, a device composed of a slab of silicon sensor material coupled with bump bonds onto a hybrid pixel detector chip. In this detector, four chips are connected to one larger sensor. The intensity measured is proportional to the energy deposited by the incoming X-ray photon. What makes Medipix detectors unique is that X-ray images can be taken at up to eight different programmable energy thresholds, which means that eight measurements with eight different threshold settings are performed within a single exposure, eliminating the need to repeat measurements eight times, which saves time and delivered radiation dose and enhancing contrast for different materials in the sample as a consequence of the different energy dependence of the respective photon attenuation. This result cannot be achieved with conventional energy-integrating detectors, where spectral information is lost [18]. In some cases, the charge deposited in a sensor may spread over a large volume, which leads to charge sharing between neighboring pixels, and an increasing number of counts, resulting in a degradation of energy resolution and errors in the photon count. To mitigate this effect, Medipix3 detectors include a mode of operation called Charge Summing Mode (CSM) that works by summing the charge deposited in overlapping clusters of four pixels and allocating the single summed hit in the pixel with the highest total charge [19]. Figure 2 shows the electronic circuitry of a Medipix3 pixel cell. The total detector is composed of a matrix of 256x256 pixel detectors with a pixel size of $55\mu m$ x $55\mu m$ with two thresholds. The eight thresholds are obtained by combining the electronics from four pixels and connecting those to one input, resulting in a pixel pitch with $110\mu m$ x $110\mu m$ spatial resolution [12] and a total detector size of $2.4mm$ x $2.4mm$.

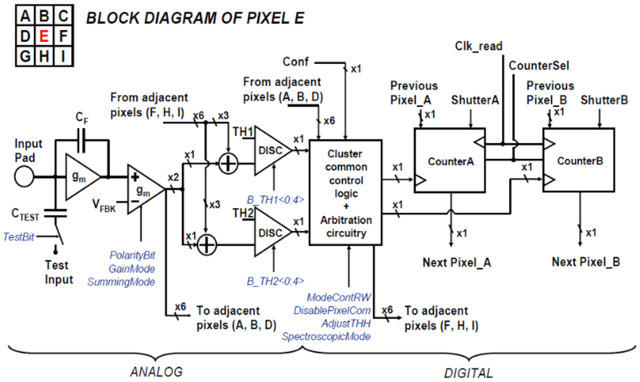

Fig. 2: *Medipix3 block diagram of a single pixel in CSM. In multispectral mode, the deposited signal is compared with the lower threshold of the pixels of the cluster, and the highest-energy pixel is selected to locate the hit. Simultaneously, adjacent summing nodes are checked for threshold exceedance by the pixel with the highest charge [12]*

For this research, the maximum tube voltage was set to 90KeV and for each image, the counts were integrated for 10000 acquisitions, which takes about 30 minutes. Table II shows the specifications of Medipix3 thresholds used for the experiments in this project.

Threshold	0	1	2	3	4	5	6	7
DAC	29	49	72	98	145	179	253	304
Energy [keV]	4	10	14.9	22.1	30	40	55	70

TABLE II: *Selected threshold DAC values and corresponding target energy*

3.2 Image formation

When the radiation emitted by the X-ray tube passes through the object, the X-rays are attenuated by the different interactions with the tissues. For a monochromatic beam, the change of intensity is described by Eq. 1

$$I = I_0 e^{-\frac{\mu}{\rho}x} \tag{1}$$

Where I is the measured object intensity, I_0 is the open beam image, $\frac{\mu}{\rho}$ is the mass attenuation coefficient, which depends on the incident energy and x is the mass per unit area, described as $x = \rho t$, ρ being the density and t the thickness of the material. Taking into account the energy (ε) dependence, we can index equation 1 as:

$$I_\varepsilon = I_{0\varepsilon} e^{-\left(\frac{\mu}{\rho}\right)_\varepsilon \rho t} \tag{2}$$

From where we can easily isolate the thickness of the material:

$$t = -\ln\left(\frac{I_\varepsilon}{I_{0\varepsilon}}\right)\frac{1}{\left(\frac{\mu}{\rho}\right)_\varepsilon \rho} \tag{3}$$

Since the absorption properties of matter are strongly dependent on the energy of the radiation, when a polychromatic X-ray beam passes through the object, lower energy photons are absorbed more strongly than higher energy ones and the average energy of the spectrum shifts towards higher values, generating an effect called beam hardening that causes softer tissues to absorb a disproportional fraction of X-rays compared to denser ones, which results in a distortion of the object shape reconstruction. When using energy bin information instead of the whole spectrum, this effect should be mitigated, since there is less variation in the spectrum.

To obtain the correct $\frac{I}{I_0}$ term for each specific energy from the acquired measurements, the following procedure was followed.

3.2.1 Energy bin images

The energy spectrum is divided into narrow bins by using the information of the eight different thresholds. The intensity corresponding to a certain energy bin $I_{\Delta\epsilon_i}$ was calculated by subtracting, for each image, the intensity of the next threshold energy as shown in Eq. 4 and represented in Fig. 3 for threshold 2.

$$I_{\Delta TH_i} = I_{TH_i} - I_{TH_{i+1}}, \quad i = 0, 1, \ldots, n-1 \tag{4}$$

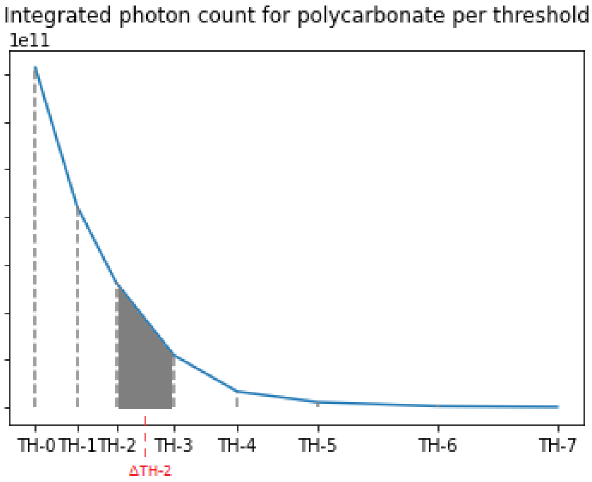

Fig. 3: *Photon counts in the detector per energy threshold. The grey bin shows the intensity of the energy bin for threshold 2 according to Eq. 4, approximated to be monochromatic for the energy corresponding to the center of the bin (red).*

3.2.2 Flat-field correction

To obtain the I_0 term, an open beam image was acquired, with no object in between the tube and the detector. With the same X-ray tube configuration and detector threshold values, an acquisition was taken before and after imaging the object. These acquisitions were averaged, and after that, the corresponding energy bin intensities for both the object and the open beam averaged images were calculated as described in section 3.2.1. Lastly, the transmission image $\frac{I}{I_0}$ was calculated for every energy by performing a per-pixel division of the object image and the averaged open beam image

3.2.3 Linear mass attenuation coefficient

The used linear mass attenuation coefficients $\frac{\mu}{\rho}$ were taken from the NIST database [20], which are calculated from the theoretical values for the total cross section per atom σ_{tot} for an interaction by the photon, and are related to μ/ρ according to equation 5

$$\mu/\rho = \sigma_{\text{tot}}/uA \tag{5}$$

Where $u = 1.660540210^{-24}$ gr [21] is the atomic mass unit and A is the relative atomic mass of the target element.

The cross-section (σ) represents the probability that photons interact with matter by a particular process. The total cross-section σ_{tot} is the sum over contributions from the principal photon interactions

$$\sigma_{tot} = \sigma_{pe} + \sigma_{coh} + \sigma_{incoh} + \sigma_{pair} + \sigma_{trip} + \sigma_{ph.n} \tag{6}$$

where σ_{pe} is the photoelectric cross section, σ_{coh} is the coherent (Rayleigh) scattering cross section, σ_{incoh} the incoherent (Compton) scattering cross section,σ_{pair} and σ_{trip} are the cross sections for electron-positron production in the fields of the nucleus and the atomic electrons, respectively, and $\sigma_{ph.n}$ is the photonuclear cross section. Figure 4 shows an example of the contribution of each significant process in the studied energy ranges for Carbon. For this project, only the contribution of the photoelectric effect was taken into account, since it is the main type of interaction in the specific energy ranges studied. Pair production and photonuclear contribution are not considered since they occur at much higher energies. Coherent Scattering is orders of magnitude smaller so can be neglected. The case of Incoherent Scattering is not taken into account because the effective contribution of this process is yet to be analyzed, and in the case that it would introduce a big error, it can be characterized and systematically corrected.

Table I shows the different μ/ρ values for polycarbonate, PEEK, graphite, PVC, and Teflon for different energies in the range of energies used in the image acquisition process.

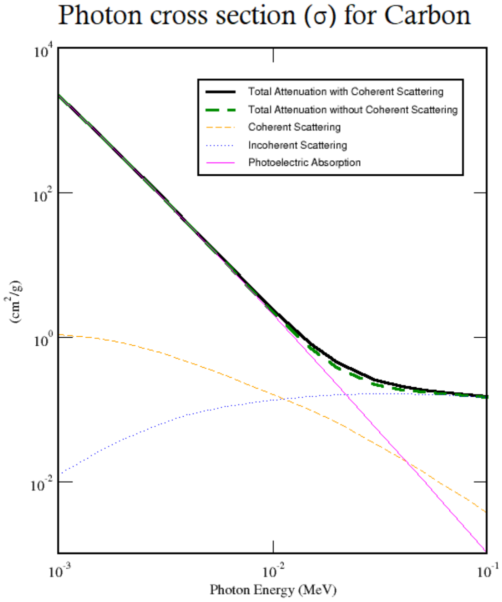

Fig. 4: *Photon cross-section data for the processes of Coherent and Incoherent Scattering and Photoelectric Absorption for Carbon.*

3.3 Energy-threshold calibration

The attenuation coefficient, photon interaction cross-sections, and related quantities are functions of the photon energy. For that reason, to obtain the right coefficient, a precise value of the energy is needed. In the Medipix3 detectors, Digital-to-Analog Converter (DAC) values are configured, which are values that are supposedly linearly related to the effective energy of the threshold value. However, the effective energy threshold might not correspond with the DAC target energy value because of inherent variability and inaccuracies in the Medipix3 detector's response to X-ray introduced by manufacturing variations, temperature, and environmental factors, or even drift over time due to electronic noise and signal processing. This energy response calibration can be accurately done using X-ray fluorescence [22]. For this project, a faster and simpler calibration method that is less accurate was developed based on measurement from a reference known material with a known thickness. A slab of polycarbonate ($C_{15}H_{16}O_2$) and plexiglas ($C_5O_2H_8$) were imaged using the energies in table I. The above mentioned energy bin 3.2.1 and flat field 3.2.2 corrections were performed on the image. Then, the linear attenuation coefficient was isolated from Eq. 2 as shown in Eq. 7.

$$(\mu/\rho)_\varepsilon = -\ln\left(\frac{I_\varepsilon}{I_{0\varepsilon}}\right)\rho t \tag{7}$$

Knowing the thicknesses of the slabs $t_{polycarbonate} = 0.3cm$ and $t_{plexiglas} = 0.2cm$, the theoretical $\frac{\mu}{\rho}$ values corresponding to various energies from NIST database, and given the logarithmic correlation between them as shown in figure 5, a per-pixel logarithmic interpolation was performed. Based on the measured attenuation, a look-up table was obtained for each pixel, that contains the effective energy of each energy bin. This is used for selecting the linear attenuation coefficient value in calculations for later acquisitions, assuming that the energy bins used are monochromatic.

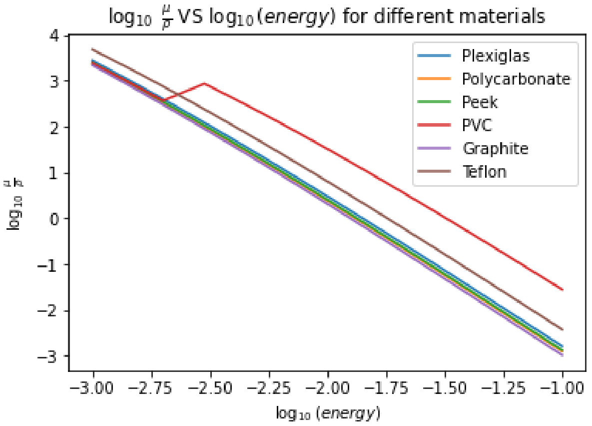

Fig. 5: *Theoretical values of* $log_{10}(\frac{\mu}{\rho})$ *VS* $log_{10}(energy)$ *for all materials. from NIST database [20].*

To test this calibration method, a piece of PEEK plastic was imaged to reconstruct its shape and calculate its volume from the acquired intensities. An additional purpose of reconstructing the shape of the PEEK sample is to qualitatively assess if beam hardening effects are still present after calculating the energy-bin images, and show as shape distortions. Figure 6 shows a phantom of the shape created from the measurements of the object.

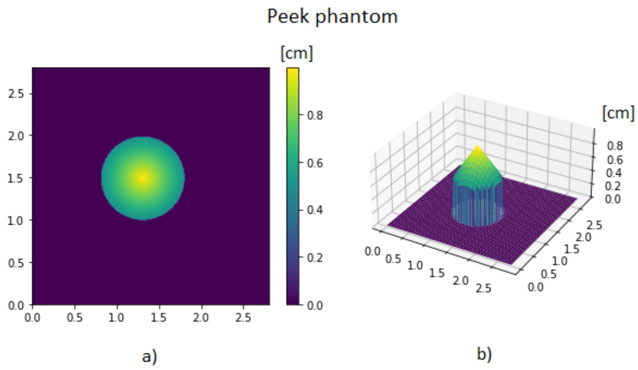

Fig. 6: *a) 2D and b) 3D shapes of the PEEK plastic sample.*

The thickness per pixel was calculated using the image processing pipeline described in section 3.2 and the μ/ρ values after calibrating.

3.4 Material decomposition

For this experiment, three different materials were glued and imaged so that the whole Field of View was covered, with areas containing an individual material, areas containing an overlap of two materials, and a central area containing an overlap of the three of them. The materials that compose the sample are PVC (C_2H_3Cl), Graphite (C), and Teflon (C_2F_4) with respective thicknesses of 0.3, 0.3, and 0.2cm. For an object composed of different separate materials, Eq. 2 can be extended into Eq. 8

$$I_\varepsilon = I_{0\varepsilon} e^{\sum_{i=0}^{m} -\left(\frac{\mu}{\rho}\right)_{\varepsilon i}\rho_i t_i} \tag{8}$$

Where m is the number of materials. In the case of this experiment, with three materials $grapite \equiv a$, $teflon \equiv b$ and $PVC \equiv c$ taking into account that Medipix3 detectors have 8 energy thresholds

$$-\ln\left(\frac{I}{I_0}\right)_0 = (\mu/\rho)_{0a}\rho_a t_a + (\mu/\rho)_{0b}\rho_b t_b + (\mu/\rho)_{0c}\rho_c t_c \tag{9a}$$

$$-\ln\left(\frac{I}{I_0}\right)_1 = (\mu/\rho)_{1a}\rho_a t_a + (\mu/\rho)_{1b}\rho_b t_b + (\mu/\rho)_{1c}\rho_c t_c \tag{9b}$$

$$\vdots$$

$$-\ln\left(\frac{I}{I_0}\right)_7 = (\mu/\rho)_{7a}\rho_a t_a + (\mu/\rho)_{7b}\rho_b t_b + (\mu/\rho)_{7c}\rho_c t_c \tag{9c}$$

To solve the system of Eq. 9, only the information for three acquisitions is needed. Then, it can be solved by applying matrix inversion. The information from the remaining acquisitions could be used to perform matrix pseudo inversion, which is a more robust method. However, the method might be extended to separate more than three materials in further experiments

3.4.1 Simulations

Before applying this method to real data, it was first tested by simulating the intensity factor for each energy. The thicknesses of the simulated object per pixel were assigned using morphological operations from the three material images to create a phantom almost equal to the actual sample. Random uniform noise with values $[0, 10^{-5}]$ was also added in the phantom to estimate the effect of inaccuracies in image acquisition in the material decomposition process.

3.5 Bone Imaging

A bone sample from a pig was obtained and imaged as a visual first approach to assess the suitability of the energy ranges selected. The sample consisted of thin silvers of pg bone, cooked and cleaned until visually free of other tissues.

3.6 Bad pixel handling

During the data acquisition process, some damaged pixel detectors might introduce corrupted data into the obtained images. Additionally, during the data preparation process described in this section, per-pixel image operations were performed. These processes include, among other operations, value subtraction and logarithmic calculations that may lead to extremely small values that when used as division terms, may computationally crash and lead to NaN and inf values.

To handle this limitation, every calculation includes a later array cleaning step in which all found corrupted pixels are given a numeric value based on the average of the adjacent non-corrupted pixels. In the case that no unspoiled neighbor pixels are available, the data is iteratively cleaned until all pixels are fixed. In this process, all corrected pixel locations were displayed and supervised.

4. RESULTS

This section shows the visual and quantitative results of implementing the methods described in the section 3.

4.1 Energy-threshold calibration

Graph 7 shows, for every threshold, a comparison of the target energy of the introduced DAC values and the mean and standard deviation (σ) of the effective energy obtained using the calibration method with plexiglas and with polycarbonate. The results deviate significantly from the target value showing lower means calculated values than the target energy, with an increasing tendency until threshold 5, where the mean energy starts to drop and the deviation starts to increase.

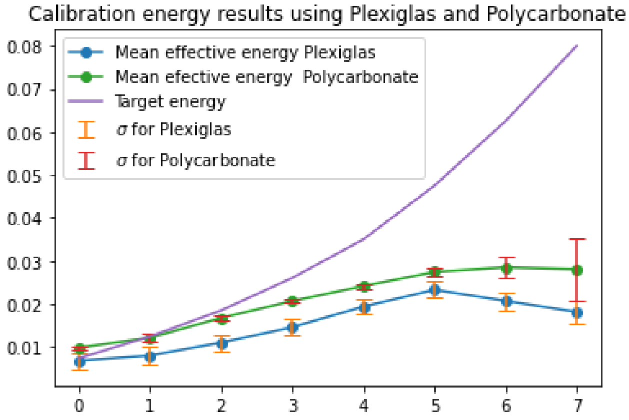

Fig. 7: *Target energy of the DAC values (purple) and mean and std effective energies of the arrays for each threshold using plexiglas (blue) and polycarbonate (green)*

Using the obtained energy values to pick the μ/ρ coefficients for the peek plastic sample, image 8 shows an example of the per-pixel thickness reconstruction using no calibration, and using plexiglas and polycarbonate as calibration materials for bin 2.

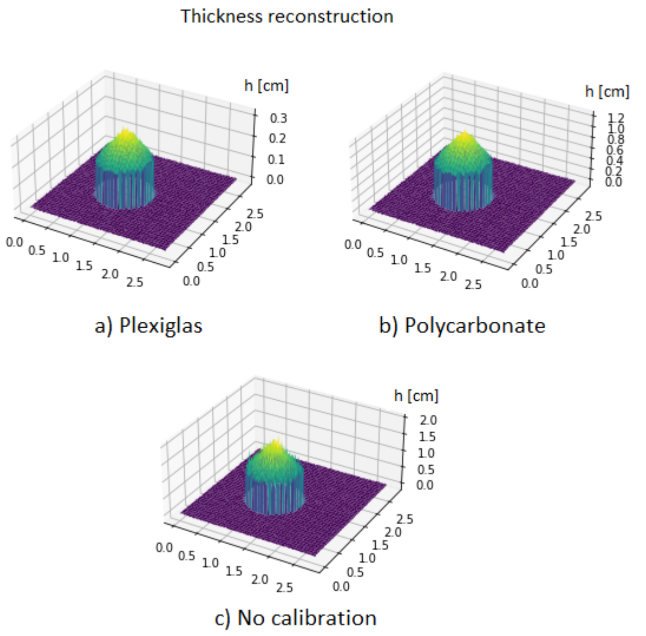

a) Plexiglas

b) Polycarbonate

c) No calibration

Fig. 8: *Examples of thickness reconstruction height [cm] with the values obtained calibrating with a) plexiglas and b) polycarbonate and c) the target values for images of bin 2. Axes x and y represent the position in the pixel array.*

The reconstructed shapes are in agreement with the expected shape 6 and show that the shape of the top is more evenly reconstructed when using any of the two calibration materials than when using the target values and no big distortions are present. Table III shows the calculated volumes averaged for all energies for the phantom (ground truth), and the reconstructions using the μ/ρ values obtained from the calibration using plexiglas and polycarbonate. No calibration means using the target values for the full array. The reconstructions with reference materials for calibration show values close to the phantom volume, in comparison with the reconstruction without calibration, which gives a volume an order of magnitude bigger than the expected value.

Object	**Volume** [cm^3]
Phantom	0.5236
Reconstruction calibrated with plexiglas	0.2871
Reconstruction calibrated with polycarbonate	0.8424
Reconstruction with no calibration	5.4970

TABLE III: *Real and calculated mean volumes for all energies for peek plastic sample using the different calibration method materials.*

4.2 Three plastic decomposition

Image 9 shows the image processing sequence for the raw image of the three overlapped materials and the open beam image. The final processed image to be analyzed in the material decomposition stage is shown in Image 10. Comparing the final processed image with the raw three material images 19 c), the image shows less noise and better contrast, along with an almost complete disappearance of the crossing straight lines where the detectors are joined. Darker values imply fewer counts, and the pixels showing extremely bright or dark values have been checked manually and do not correspond to corrupted values, but simply to proportionally big or small values in the data.

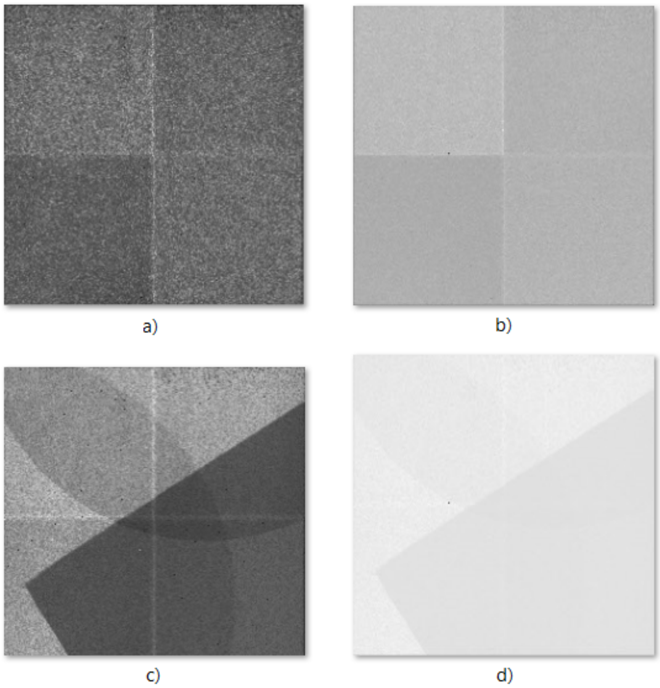

Fig. 9: *Examples of the image operations sequence for threshold 3. The figures show the a) averaged open beam image, b) averaged open beam energy bin image, c) raw materials image, d) materials energy bin image for threshold 3*

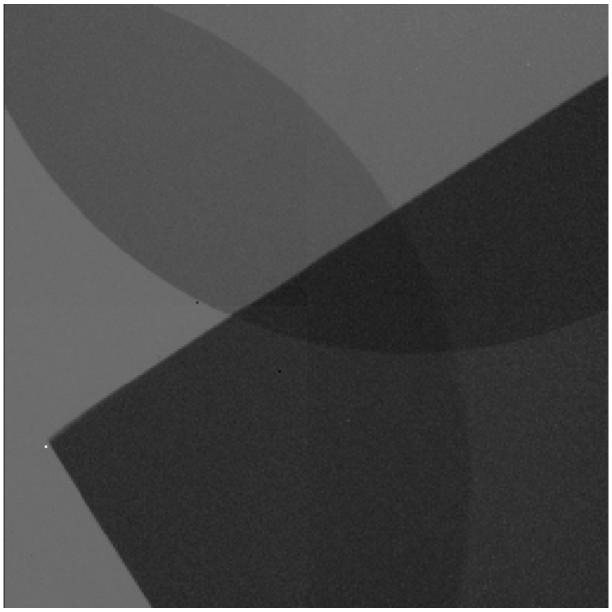

Fig. 10: *Final processed image for threshold 3 used for material decomposition.*

The full set of processed images for all thresholds can be found in Appendix 1

4.2.1 Simulation

The material decomposition method gives the material separation shown in Fig 11 for simulated acquisition data and with and without additional noise. The method perfectly separates the materials for the simulated data, showing a clear distinction between the three materials and showing their shape and the expected calculation for thickness. In the case of added noise to the simulated data, PVC material is perfectly distinguished while graphite and teflon show noise in the reconstructed thickness.

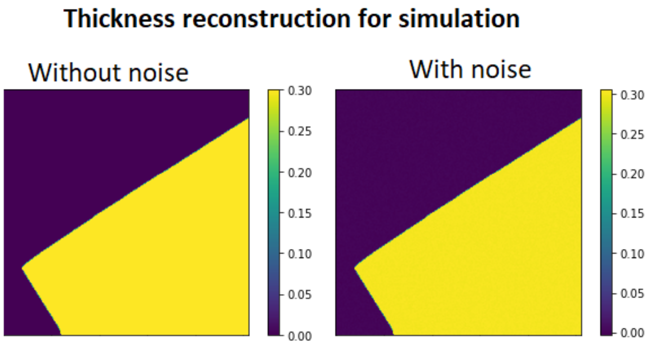

a) PVC

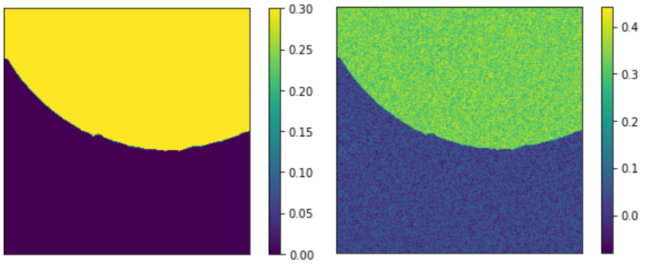

b) Graphite

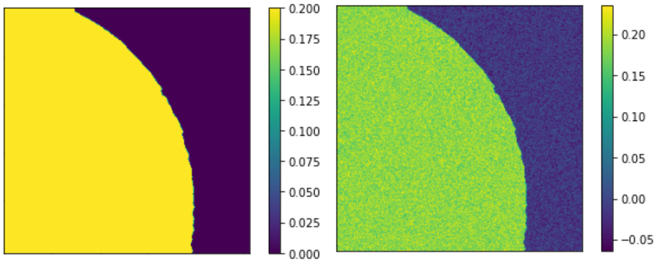

c) Teflon

Fig. 11: *Thickness reconstruction [cm] for a) PVC b) Graphite and c) Teflon materials for the simulated data with (right) and without (left) adding noise.*

Table IV shows the proportion of each material calculated from the thickness reconstructions of each material.

Reconstruction proportions for	PVC	Graphite	Teflon
Simulation	0.36	0.34	0.30
Simulation with noise	0.34	0.40	0.26
Data calibrated with Plexiglas	0.02	0.66	0.32
Data calibrated with Polycarbonate	0.02	0.39	0.59
Data with no calibration	0.04	0.90	0.06

TABLE IV: *Proportions of PVC, Graphite, and Teflon for the reconstructed thicknesses of the simulated data with and without the added noise.*

4.3 Bone Imaging

An example of the processed images applying energy bin and flat field correction for all thresholds is shown in Fig. 12. These images show a clear distinction in the number of detected photons and bone textures and features for the different energy bins (like the line visible in bins 2, 3, and 4). Note that the bone sample is wrapped in plastic which is an added material to the sample. In this case, it is not taken into account since no further calculations are performed due to the lack of information in terms of the material composition of the bone sample.

5. DISCUSSION

To calibrate for the correct energy thresholds that the detectors are measuring, the corrections were performed using an approach that assigns pixel-wise a μ/ρ value corresponding to reconstructing the known thickness of an imaged sample, and later perform a logarithmic interpolation to assign an energy value using the information from NIST database for plexiglas and polycarbonate materials. Only the photoelectric effect was considered as a contributor to the cross-section, however, Compton scattering might also be contributing, resulting in high-energy photons showing as low energy ones. The amount of Compton scattered photons that reach the detector can be corrected with an anti-scatter grid, but that will not remove the scattered photons in the sample, which requires high-order corrections. The effect of Compton scattering is still to be studied and should be taken into account in the cross-section. The calculated mean effective energies per threshold plotted in a graph 7 show, for plexiglas, a decay in energy from threshold 5 on. This should not happen since each threshold has an increasing target energy. In the case of polycarbonate, the deviation from, the mean increases considerably, so the data is showing inconsistencies in the form of noise. For this reason, the measurements from threshold 5 on will be left out in the material decomposition procedure. For the rest of the energies, the values are, except for threshold 0, smaller than the target one, which could imply fluctuations in the X-ray source that might affect the energy distribution of the emitted X-rays or a bad characterization of the detector response. The deviations from the mean value are generally not bigger than the size of the bin, so they should not be a source of error. Fig. 8 shows that the shape is less noisy when using any of the two calibration materials. In general, no important edge distortions are shown, which suggests that beam hardening is well accounted for in the energy-bin calculation step. However, there is a big overestimation of thickness when no calibration is performed, which also shows in the resulting volume in Table III. The best reconstructions for a peek sample in terms of shape and volume are obtained using any of the reference calibration materials. This method is a simplification of the calibration proposal by A. Brambilla et al. [23] that has already demonstrated to have many limitations. To better calibrate these values, an X-ray fluorescence analysis could be performed, which is a good source of calibration spectra with well-defined photon energies.

As for the material decomposition part, the proposed pipeline has the potential to accurately differentiate overlapped materials as shown in Fig.11 (left), for simulated data where all thicknesses were correctly reconstructed, demonstrating the accuracy of the equations proposed. However, matrix inversion as the analytical solution is very sensitive to noise in the data. This is well reflected in Fig. 8 (right), where 0-0.00001% noise uniformly added to the data significantly modifies the results in terms of separation of materials. On the other hand, when applying the described pipeline to the real acquired data, the material decomposition method gives inconsistent results that do not match with the expected proportions, as compared in table IV. This could be due to accumulated errors in the calculation pipeline, where the energy bins are considered monochromatic but that however do have a certain width that introduces variability in the data. At the same time, the four detectors that compose Medipix3 can result in different intensity ranges because of manufacturing differences. The gap between detectors is especially visible in the raw data and is not completely corrected in the flat-field correction step, as show in the example in Fig. 10. Additionally, the glue used for sticking the materials together might contain heavy materials that interfere with the imaging, and its composition and contribution should be studied before using it.

To use Medipix3 detectors in the task of characterization of healthy bone samples, to better assess BMD measurements in the future, still many limitations need to be addressed. Images in example 12 show that the bones of an animal are visible and show different responses for different energies, which suggests that the chosen energy ranges for this experiments might be suitable for this task. However, with the current analysis, the Medipix3 detectors are not yet suitable for looking at unknown bone samples. With no previous hypothesis of the composition of the tissues or no accurate ground truth of their proportion, this method is not applicable. Once the current limitations for planar X-ray imaging are overcome, an extension to this research should aim to extend the imaging technique to 3D CT, obtaining more detailed information on the tissue composition. With a 3D CT pipeline and a hypothesis of the specific tissues that compose the bone, the goal would be to build a dataset from healthy patient samples that include the standard values of the density of each tissue that composes the bone. With this information an assessment of the deviation from healthy

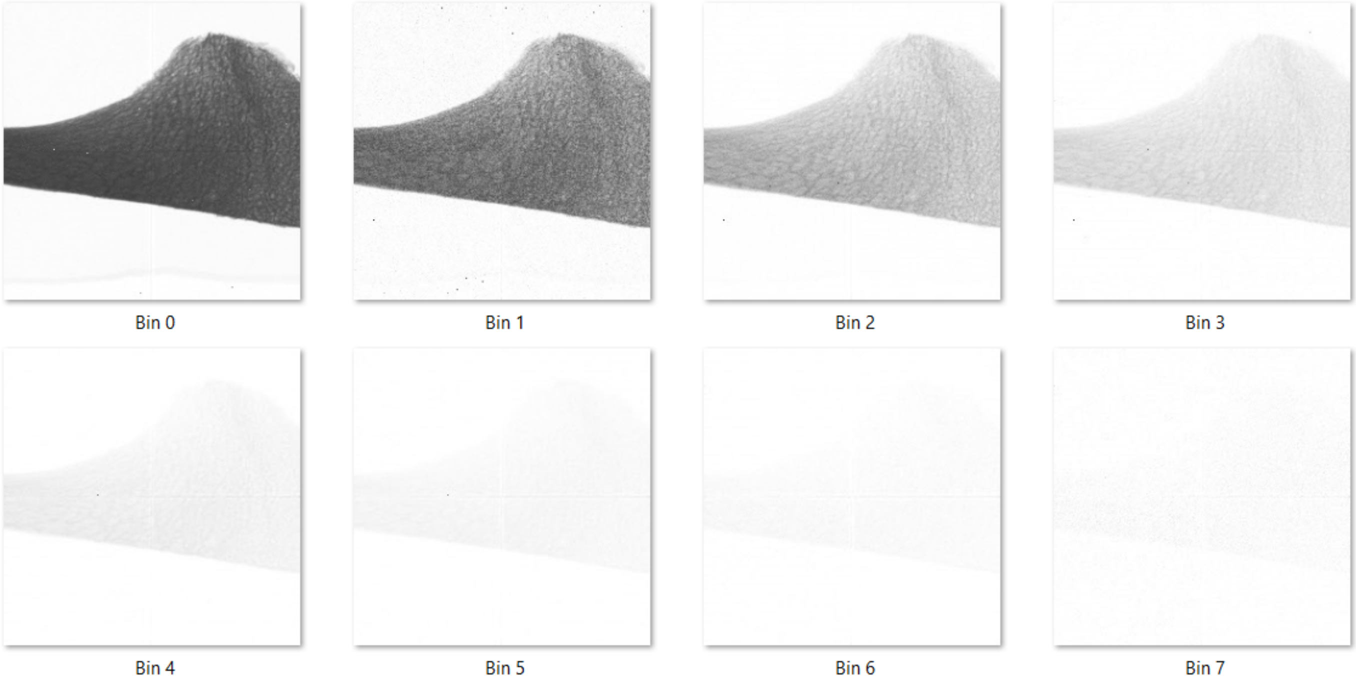

Fig. 12: *Corrected images for bone samples in all energy bins.*

values of certain tissues could be performed when a patient is undertaking a dual-energy CT scan, contributing to the early diagnosis of osteoporosis.

To make this set-up suitable for testing for bone samples and obtaining reliable information, further analysis should be conducted by imaging different samples with different properties and analyzing if the deviations are consistent through the measurements and in that case systematically correct for those.

6. CONCLUSION

This project presents a first approach to the feasibility of using multispectral Medipix3 detectors in the task of generating a 'golden standard' dataset for bone mineral composition to properly determine the bone mineral density (BMD) from patients with a CT scan, with the objective of a better diagnosis of osteoporosis disease, taking advantage of the high resolution and photon-counting technology of these detectors. The experiments have focused on the step of material decomposition for known material samples in 2D using X-rays. A pipeline was presented in which first, a calibration method was developed for the threshold energy values based on the expected values from reference materials. The results tested on a peek sample show that this calibration method improves the reconstruction shape and volume although it has some limitations that could be addressed by using a more accurate calibration method such as fluoroscopy X-Ray. In the task of material separation, results have shown that Medipix3 detectors have a lot of potential, but that the data processing and set-up calibration is not trivial. Further research should be extended, including analysis that studies the effect of Compton scattering and other systematic errors that can be corrected, with the further goal of imaging the samples using CT technique and building a 'golden dataset' that contains information on the composition of tissues in bones for healthy patients.

This research has demonstrated that that the Medipix3 detector can be used for material separation analyzing its potentials and limitations and proposing the further steps that need to be taken for a proper measurement of bone quality, demonstrating once more the versatility of Medipix3 detectors in the different fields outside high-energy physics.

BIBLIOGRAPHY

[1] Emma Hernlund et al. "Osteoporosis in the European Union: medical management, epidemiology and economic burden: a report prepared in collaboration with the International Osteoporosis Foundation (IOF) and the European Federation of Pharmaceutical Industry Associations (EFPIA)". In: *Archives of osteoporosis* 8 (2013), pp. 1–115.

[2] Olof Johnell and JA Kanis. "An estimate of the worldwide prevalence and disability associated with osteoporotic fractures". In: *Osteoporosis international* 17 (2006), pp. 1726–1733.

[3] Glen M Blake and Ignac Fogelman. "The role of DXA bone density scans in the diagnosis and treatment of osteoporosis". In: *Postgraduate medical journal* 83.982 (2007), pp. 509–517.

[4] MK Garg and Sandeep Kharb. “Dual energy X-ray absorptiometry: Pitfalls in measurement and interpretation of bone mineral density”. In: *Indian journal of endocrinology and metabolism* 17.2 (2013), p. 203.

[5] HH Bolotin. “DXA in vivo BMD methodology: an erroneous and misleading research and clinical gauge of bone mineral status, bone fragility, and bone remodelling”. In: *Bone* 41.1 (2007), pp. 138–154.

[6] M Darryl Antonacci, Darrell S Hanson, and Michael H Heggeness. “Pitfalls in the measurement of bone mineral density by dual energy x-ray absorptiometry”. In: *Spine* 21.1 (1996), pp. 87–90.

[7] Daniel Chappard et al. “New laboratory tools in the assessment of bone quality”. In: *Osteoporosis International* 22 (2011), pp. 2225–2240.

[8] Nicholas Mikolajewicz et al. “HR-pQCT measures of bone microarchitecture predict fracture: systematic review and meta-analysis”. In: *Journal of Bone and Mineral Research* 35.3 (2020), pp. 446–459.

[9] Joshua A MacNeil and Steven K Boyd. “Accuracy of high-resolution peripheral quantitative computed tomography for measurement of bone quality”. In: *Medical engineering & physics* 29.10 (2007), pp. 1096–1105.

[10] APH Butler et al. “Bio-medical X-ray imaging with spectroscopic pixel detectors”. In: *Nuclear Instruments and Methods in Physics Research Section A: Accelerators, Spectrometers, Detectors and Associated Equipment* 591.1 (2008), pp. 141–146.

[11] Doniyor Jumanazarov et al. “Material classification using basis material decomposition from spectral x-ray CT”. In: *Nuclear Instruments and Methods in Physics Research Section A: Accelerators, Spectrometers, Detectors and Associated Equipment* 1056 (2023), p. 168637.

[12] CERN Medipix Collaboration. *Medipix3 Website*. Retrieved from https://medipix.web.cern.ch/medipix3. 2005.

[13] Katsuyuki Taguchi and Jan S Iwanczyk. “Vision 20/20: single photon counting x-ray detectors in medical imaging”. In: *Medical physics* 40.10 (2013), p. 100901.

[14] Martin J Willemink et al. “Photon-counting CT: technical principles and clinical prospects”. In: *Radiology* 289.2 (2018), pp. 293–312.

[15] Nikhef - Dutch National Institute for Subatomic Physics. *Nikhef Website*. https://www.nikhef.nl/en/.

[16] UMCU - University Medical Center of Utrecht. *UMCU Website*. https://www.umcutrecht.nl/nl/.

[17] Jerrold T Bushberg and John M Boone. *The essential physics of medical imaging*. Lippincott Williams & Wilkins, 2011.

[18] Rafel Ballabriga Suñé. “The design and implementation in 0.13¿ m cmos of an algorithm permitting spectroscopic imaging with high spatial resolution for hybrid pixel detectors”. PhD thesis. Universitat Ramon Llull, 2009.

[19] R Ballabriga et al. “Characterization of the Medipix3 pixel readout chip”. In: *Journal of Instrumentation* 6.01 (2011), p. C01052.

[20] *NIST database*. https://physics.nist.gov/PhysRefData/Xcom/html/xcom1.html.

[21] E Richard Cohen and Barry N Taylor. “The 1986 adjustment of the fundamental physical constants”. In: *Reviews of Modern Physics* 59.4 (1987), p. 1121.

[22] HM Cho et al. “Energy response calibration of photon-counting detectors using x-ray fluorescence: a feasibility study”. In: *Physics in Medicine & Biology* 59.23 (2014), p. 7211.

[23] A Brambilla et al. “Basis material decomposition method for material discrimination with a new spectrometric X-ray imaging detector”. In: *Journal of Instrumentation* 12.08 (2017), P08014.

APPENDIX

Energy [MeV]	μ/ρ $[cm^2/gr]$					
	Polycarbonate	**Plexiglas**	**PEEK**	**Graphite**	**PVC**	**Teflon**
1.000E-03	2.792E+03	2.496E+03	2.387E+03	2.454E+03	2.210E+03	4.823E+03
1.500E-03	9.143E+02	8.057E+02	7.690E+02	8.216E+02	6.994E+02	1.670E+03
2.000E-03	4.027E+02	3.519E+02	3.354E+02	3.709E+02	3.017E+02	7.589E+02
3.000E-03	1.228E+02	1.062E+02	1.010E+02	8.687E+02	8.965E+01	2.401E+02
4.000E-03	5.184E+01	4.453E+01	4.233E+01	4.126E+02	3.724E+01	1.036E+02
5.000E-03	2.628E+21	2.247E+21	2.134E+21	2.276E+21	1.866E+21	5.335E+21
6.000E-03	1.499E+21	1.277E+21	1.212E+21	1.386E+21	1.054E+21	3.081E+21
8.000E-03	6.114E+21	5.181E+21	4.913E+21	6.204E+21	4.241E+21	1.279E+21
1.000E-02	3.025E+21	2.552E+21	2.419E+21	3.280E+21	2.076E+21	6.411E+21
1.500E-02	8.278E+21	6.940E+21	6.569E+21	1.001E+21	5.585E+21	1.794E+21
2.000E-02	3.263E+21	2.723E+21	2.576E+21	4.233E+21	2.177E+21	7.170E+21
3.000E-02	8.668E+21	7.199E+21	6.804E+21	1.228E+21	5.706E+21	1.938E+21
4.000E-02	3.360E+21	2.781E+21	2.627E+21	5.030E+21	2.193E+21	7.591E+21
5.000E-02	1.606E+21	1.327E+21	1.253E+21	2.501E+21	1.042E+21	3.656E+21
6.000E-02	8.773E+21	7.236E+21	6.831E+21	1.407E+21	5.671E+21	2.007E+21
8.000E-02	3.378E+21	2.780E+21	2.623E+21	5.657E+21	2.169E+21	7.787E+21
1.000E-01	1.613E+21	1.325E+21	1.250E+21	2.782E+21	1.031E+21	3.738E+21

TABLE I: *μ/ρ values for polycarbonate, plexiglas, graphite, PVC, and teflon for different energy values.*

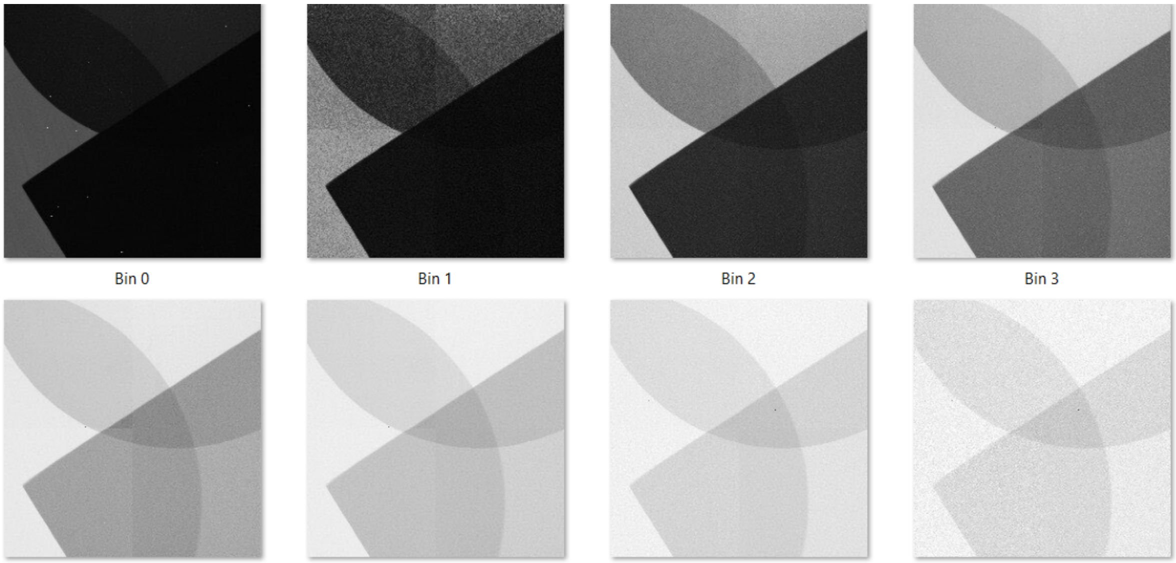
Bin 0 Bin 1 Bin 2 Bin 3
Bin 4 Bin 5 Bin 6 Bin 7

Fig. 1: *Final processed images of materials for all energy bins*